

# Characterization of the fast ionization wave induced by a CO<sub>2</sub> laser pulse in argon

Cite as: J. Appl. Phys. **126**, 243304 (2019); <https://doi.org/10.1063/1.5115815>

Submitted: 24 June 2019 . Accepted: 30 November 2019 . Published Online: 23 December 2019

Kohei Shimamura , Ippei Yokota, and Shigeru Yokota



View Online



Export Citation



CrossMark

## ARTICLES YOU MAY BE INTERESTED IN

[Electron extraction enhancement via the magnetic field in a miniature microwave discharge neutralizer](#)

Journal of Applied Physics **126**, 243302 (2019); <https://doi.org/10.1063/1.5127805>

[Two-dimensional particle simulation on the behavior of multi-charged copper ions in the cathode spot of a pulsed vacuum arc discharge](#)

Journal of Applied Physics **126**, 243303 (2019); <https://doi.org/10.1063/1.5125223>

[Internal quantum efficiency measurements in InAs/GaSb superlattices for midinfrared emitters](#)

Journal of Applied Physics **126**, 243101 (2019); <https://doi.org/10.1063/1.5129163>



## Your Qubits. Measured.

Meet the next generation of quantum analyzers

- Readout for up to 64 qubits
- Operation at up to 8.5 GHz, mixer-calibration-free
- Signal optimization with minimal latency

Find out more



# Characterization of the fast ionization wave induced by a CO<sub>2</sub> laser pulse in argon

Cite as: J. Appl. Phys. 126, 243304 (2019); doi: 10.1063/1.5115815

Submitted: 24 June 2019 · Accepted: 30 November 2019 ·

Published Online: 23 December 2019



Kohei Shimamura,<sup>a)</sup>  Ippei Yokota, and Shigeru Yokota

## AFFILIATIONS

Department of Engineering Mechanics and Energy, University of Tsukuba, 1-1-1 Tennodai, Tsukuba Ibaraki 305-8573, Japan

<sup>a)</sup>Author to whom correspondence should be addressed: [shimamura@kz.tsukuba.ac.jp](mailto:shimamura@kz.tsukuba.ac.jp)

## ABSTRACT

Fast ionization wave (FIW), a postbreakdown phenomenon of laser-induced plasma, is observed for a laser intensity of  $10^{11}$ – $10^{13}$  W/m<sup>2</sup> using the CO<sub>2</sub> laser pulse in the atmospheric pressure condition. FIW is distinguishable as “overdriven detonation” according to Raizer’s Chapmann-Jouguet detonation theory because FIW is known as the type of laser-absorption wave that has a higher propagation velocity than the laser-supported detonation wave (LSDW). Some reports have described the expansion of FIW using a solid-state laser. Nevertheless, the threshold phenomena between FIW and LSDW are not fundamentally understood. This study used the high-speed visualization and optical emission spectroscopy to investigate the transition of the laser-absorption wave in argon gaseous form. To elucidate the physics of the transition threshold, a 5 J CO<sub>2</sub> pulse laser, an Echelle spectrometer, and an intensified CCD camera are used for the quantitative investigation of the plasma temperature and density. Results demonstrate that the FIW front had an electron temperature of 0.7 eV and an electron number density of  $2.5 \times 10^{23}$  m<sup>-3</sup>. At the FIW–LSDW transition, the electron temperature increased by 1 eV, and the density decreased by  $2.2 \times 10^{23}$  m<sup>-3</sup>. Besides, the transition threshold and the existence of local-thermodynamic equilibrium were evaluated based on the electron temperature, and the density was obtained from the spectroscopic experiments.

Published under license by AIP Publishing. <https://doi.org/10.1063/1.5115815>

## I. INTRODUCTION

Laser-induced plasma and shock waves propagate in different mechanisms ranging from gas breakdown to adiabatic shock wave expansion according to the focusing condition, laser wavelength, and the gaseous media that are used. The literature elucidating the laser-absorption wave describes three different types.<sup>1</sup> After laser breakdown, the type of laser-absorption wave changes to laser-supported radiation wave (LSRW), laser-supported detonation wave (LSDW), and laser-supported combustion wave (LSCW) according to the time change of the laser pulse intensity. The two types of laser-absorption waves in high-intensity laser irradiation are commonly known as the fast ionization wave (FIW) and LSRW.<sup>2</sup> In LSRW, the plasma radiation induces seed electrons of the plasma front and directly increases the number of electrons. The velocity of the ionization wave of LSRW is expressed as a function of the number density of neutral particles pouring from upstream and the ionizing photon flux coming from downstream.<sup>3</sup> In other words, the propagation of the LSRW is regulated by self-UV-radiation because this velocity has no additional heating source, such as laser irradiation and shock heated gas. This is because, in FIW, plasma radiation only induces the seed electrons of

avalanche ionization, and the role of laser irradiation is important for increasing the number of electrons.<sup>4–6</sup> Although the electric field between the streamer and laser-plasma is fundamentally different, the propagation mechanism of FIW is similar to the streamer discharge.<sup>7,8</sup> The typical ionization-wave velocity of the streamer is of the same order as the FIW. The lower bound of the FIW velocity is found as a function of plasma radiation, the photoabsorption cross section, and the intrinsic energy of the gas behind the front.<sup>2</sup> Practically speaking, the difference between FIW and LSRW depends on the ambient pressure. Fisher predicted that the threshold of the LSRW and FIW is the pressure at 0.1 atm.<sup>5</sup> Furthermore, the laser wavelength is important in generating the FIW or LSDW. The coefficients of the inverse Bremsstrahlung process are proportional to the third power of the wavelength. The long peak pulse width of the gas laser sustains easily the FIW. Several experimental examples of solid-state laser wavelengths have been identified.<sup>9–12</sup> Specifically, Harilal performed self-emission imaging and emission spectroscopic measurement with an intensified CCD (ICCD) in argon at atmospheric pressure. In the experiment, the plasma front velocity was measured to be about 30 km/s,

which is the typical velocity of the FIW. However, only a few visualization experiments using a streak camera and a CO<sub>2</sub> laser were reported in 70–80 s.<sup>13–15</sup>

The transition threshold of the laser-absorption wave is important for applications such as laser-induced breakdown spectroscopy and materials processing. For example, using a CO<sub>2</sub> laser, the breakdown threshold is 10<sup>13</sup> W/m<sup>2</sup>, the FIW–LSDW transition is 10<sup>11–12</sup> W/m<sup>2</sup>, and the LSDW–LSCW transition is 10<sup>10–11</sup> W/m<sup>2</sup> in an atmospheric air condition.<sup>16–19</sup> Raizer’s Chapmann-Jouguet (CJ) detonation theory can simplify the investigation of the transition threshold of laser-absorption waves.<sup>20</sup> LSRW and FIW have faster propagation speeds than those predicted by CJ theory: it is recognized as an overdriven detonation state in detonation theory. The LSCW velocity is lower than that of CJ theory (LSDW), i.e., it is the “combustion wave” in the context of detonation theory. However, an important shortcoming of Raizer theory is that the theoretical value can be predicted arbitrarily by the specific heat ratio. In the FIW or LSDW, it can be judged by whether the slope of the straight line on laser intensity and the velocity plane is greater than one-third of Raizer’s law. Fisher predicted the threshold model theoretically, which is an idea similar to that of the laser breakdown theory using the solution of the electron energy equation.<sup>6</sup> The FIW–LSDW threshold is a function of the electron temperature and the electron density. In an earlier report, we measured the FIW–LSDW transition threshold at 1 atm air using a high-speed camera and CJ theory.<sup>17</sup> Ascertaining the transition and propagation mechanisms from FIW to LSDW requires the elucidation of the plasma properties, especially the electron temperature and density. This study clarified the transition and propagation mechanism of the ionizing wavefront in laser-absorption waves using optical emission spectroscopy and high-speed shadowgraphy. A TEA CO<sub>2</sub> laser was used to observe the separation events of FIW and LSDW easily. For this experiment, argon was used as the atmospheric gas to conduct the chemical reaction simply and to sustain the long period of FIW.

## II. HIGH-SPEED VISUALIZATION OF TRANSITION BETWEEN FIW AND LSDW

Laser shadowgraph visualization was used to observe the FIW–LSDW transition. A transversely excited atmospheric CO<sub>2</sub> pulse laser (5 J/pulse, TEA-101; GSI Group Inc.) was used. The maximum peak power was 1.8 MW, and the peak laser pulse FWHM was 200 ns. A 90° off-axis parabolic mirror with 140 mm focusing was used to focus the laser beam on the aluminum target, which was set in a small vacuum chamber. The argon gaseous form was filled at 101.3 kPa. An Al target plate was used to generate the free electrons for cascading. No ablation occurred on the Al surface through this experimental condition. To avoid multiple breakdown along the laser beam, we reduced the laser power as 1.1 J. We also used a high-speed ICCD camera (Ultra NEO; NAC Inc.). This camera, which has a 1024 × 860 pixel resolution, can take 12 frames in each operation at 100 million frames per second (fps) and 5 ns exposure time. Figure 1(b) presents the series of the shadowgraph for the laser-induced plasma in an argon atmosphere. The exposure time for each image was 20 ns.

Figure 1 presents the series of shadowgraphs for laser-induced plasma in argon, and the Al flat-plate target was placed on the

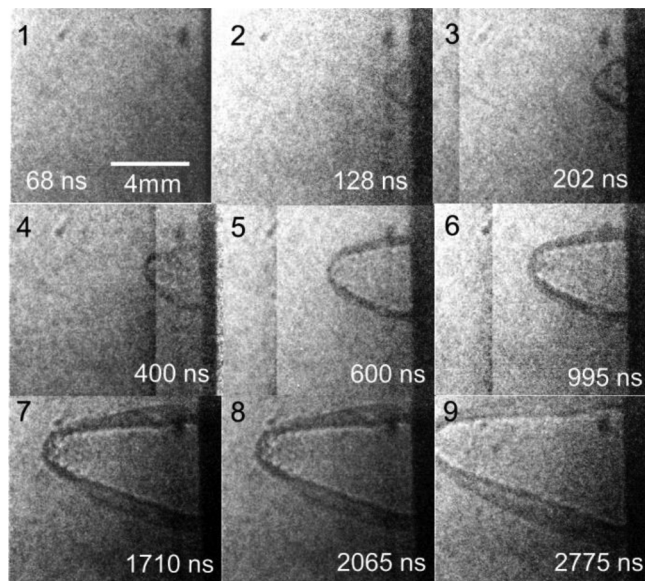


FIG. 1. Series of shadowgraph images of argon plasma for times of 68–2775 ns.

right edge of the images. The laser beam was irradiated from the left part. The plasma can be confirmed as the white body on the shadowgraph developed and expanded in the left direction of photography as time passes immediately after laser irradiation. Shock waves were generated around the plasma because of the rapid expansion. Because the shock wave also propagated perpendicularly to the laser irradiation direction, a black shadow was apparent between the shock wave and the plasma, as shown in Nos. 5–9 in Fig. 1. Figure 2 presents the ionization-wave front distance from the aluminum plate over time, in addition to the laser pulse shape. The irradiation start timing of the laser beam was 20 ns. The ionization-wave front position, as confirmed from the shadowgraph, was 27 ns. The difference from the laser pulse timing was 7 ns. Figure 3 presents the relationship between the propagation distance and the laser irradiation intensity in front of the ionization wavefront. The laser irradiation intensity was obtained from the relation between the mirror focusing-*f* number and the propagation distance.<sup>21</sup> Figure 4 depicts the relation between the ionization-wave velocity and laser intensity, which is a visual representation of the FIW–LSDW transition. In light of the fact that LSDW has data on the CJ-detonation theory line, the propagation velocity of FIW is inferred as higher than that of CJ-detonation. In other words, it is in an “overdriven detonation” state. For comparison with this experiment, earlier Boiko experiment results are shown in Fig. 4.<sup>14</sup> The presently obtained data and the Boiko data can be regarded as continuous. For a laser intensity of  $1.0 \times 10^{11}$  W/m<sup>2</sup> and an ionization velocity of 5 km/s, FIW–LSDW transition is apparent as an intersection with Raizer’s CJ theory. From Fig. 3, the FIW transition is about 200 ns after irradiation at  $1.0 \times 10^{11}$  W/m<sup>2</sup>. We can find no difference in terms of the

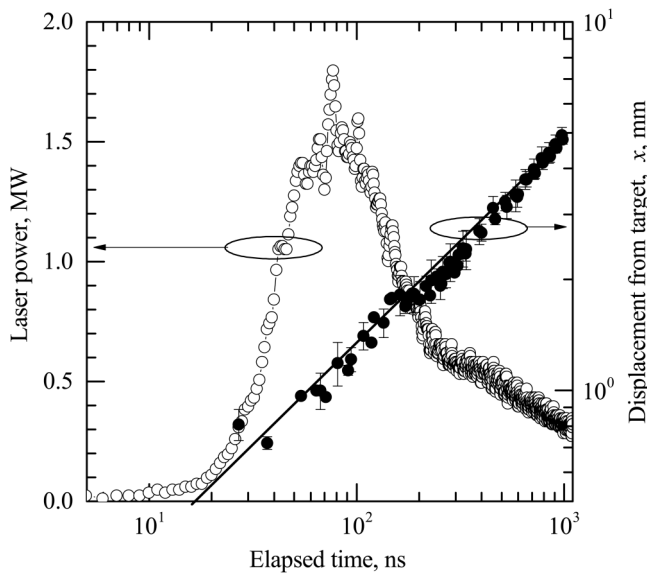


FIG. 2. Laser pulse shape and the distance between the target and the ionization front of the laser-induced plasma.

transition if we examine the front part of the wavefront around 200 ns in the shadowgraph. The shadowgraph is sensitive to the second derivative of the density space. Therefore, a discontinuous change in density can be regarded as a shadowgraph. In other words, it is difficult to ascertain from the shadowgraph whether the shock wave is ahead or the plasma is ahead. In Fig. 1, depicting an ionization wave for which  $t = 995$  ns, a black shadow line is visible in the front part, which clearly illustrates that the shock

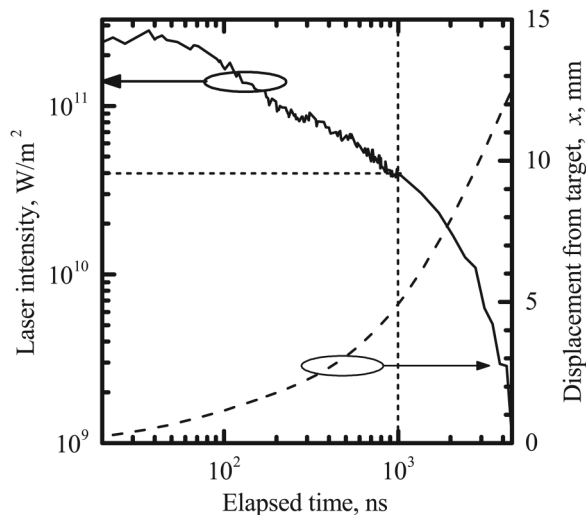


FIG. 3. Laser intensity and the displacement of the ionization wavefront.

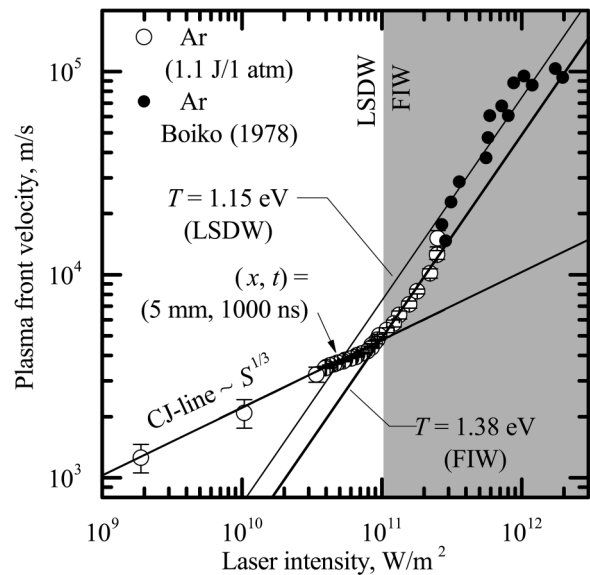


FIG. 4. Ionization wave velocity in terms of laser intensity. Raizer's CJ theory line is the solid line.

wave is in front of the plasma. Although the threshold can be discerned from the shadowgraph and detonation theory, the phenomena before and after the transition are not clarified. Furthermore, FIW and LSDW wavefront temperatures were evaluated using Raizer's Hugoniot analysis and Zeldovich's internal energy model. Raizer considers the absorption region of the plasma wavefront moving toward the laser. Such an analysis is appropriate because the absorption length is remarkably short in a long wavelength experiment such as that with a CO<sub>2</sub> laser.<sup>18</sup> It can be expressed as  $S = \rho U \epsilon(\bar{m}, T)$  from energy conservation based on the assumption that the particles in the control volume absorb all the laser energy.<sup>20</sup> Here,  $U$  represents the velocity of the wavefront. Also,  $\epsilon(\bar{m}, T)$  and  $\bar{m}$  are, respectively, the internal energy of the particle in the absorption layer and the average charge of plasma,<sup>22</sup>

$$\epsilon(\bar{m}, T) = \frac{3}{2}nk(1 + \bar{m})T + n \sum g_i E_i \exp\left(-\frac{E_i}{kT}\right). \quad (1)$$

Here,  $n$  is the particle number density in the absorption layer and the internal energy included the excitation energy assuming Boltzmann's distribution.<sup>23</sup> The excitation energy model consists of 31 energy level  $E_i$  and statistical weight  $g_i$ .<sup>24</sup> Using Eq. (1) and control volume analysis, the temperature can be obtained with the iterative calculation. As a result, the data plots of FIW on the  $S-U$  plane in the present study corresponded to the temperature estimated line at 1.38 eV. For LSDW at  $(x, t) = (5 \text{ mm}, 1000 \text{ ns})$ , the estimated temperature line was 1.15 eV, which was the intersection of the estimated temperature line and the CJ theory line.

### III. OPTICAL EMISSION SPECTROSCOPY

#### A. Experimental setup

To obtain the electron temperature and density, we used an Echelle spectrometer (*f*/7, 195 mm focal length, Mechelle 5000; Andor Technology) with an ICCD camera (1024 × 1024 pixel resolution, 5 ns minimum exposure time, iStar DH334T-18F-E3; Andor Technology) with spectral resolution  $\lambda/\Delta\lambda$  being 6000 for wavelengths of 250 nm and 975 nm. Wavelength calibration was conducted using a xenon pencil style spectral calibration lamp (6033; Newport Corp.). A standard of the spectral irradiance tungsten lamp (OL245 M; Optronic Laboratories, Inc.) was used for intensity calibration. The spectrometer gates and laser operations were controlled using a pulsed-delay generator (DG535; Stanford Research Systems Inc.), which first receives a trigger signal from the lasers. After adding a delay, it triggers the camera and the shutter controller. The ICCD gate time was 100 ns. Irradiation of the plasma was corrected using 100-mm-diameter lenses with a 150 mm focal length. The focal spot diameter at the spectroscopic measurement point was 1 mm. To clarify the state of plasma expansion,  $x = 0.5$  mm (0–1 mm) for FIW and  $x = 5.0$  mm (4.5–5.5 mm) for LSDW, where the plasma propagation can be confirmed mostly from the shadowgraph.

#### B. Continuum radiation analysis

In the emission spectrum in the early stage of the breakdown of laser-induced plasma, a line spectrum and a continuous spectrum are observed simultaneously. Here, the method of analyzing the continuous spectrum is summarized. The continuous spectrum is divided into the Bremsstrahlung process (free-free) in which electrons are decelerated by heavy particles such as ions and neutral particles and bound-free because of recombination of electrons and ions. Then, the overall volumetric energy continuum emission  $J$  is presented below:

$$J = \int j_{\nu} d\nu = \int j_{ff\nu} d\nu + \int \sum j_{fb\nu} d\nu. \quad (2)$$

Here, for free-bound emission, one must consider each energy level. It is a total form. First, free-free emission is discussed mainly in the wavenumber space in the literature, but the actual emission spectrum is observed in the wavelength space rather than the wavenumber space. Using  $d\nu = c\lambda^{-2}d\lambda$ , the wavenumber-wavelength relation can be rewritten as expressed below,<sup>23</sup>

$$j_{ff\lambda} d\lambda = \frac{Z^2 e^6}{3\sqrt{3}\pi c^2 (2\pi m_e)^{1.5} \epsilon_0^2 \sqrt{kT_e}} \frac{n_i n_e}{\lambda^2} \exp\left(-\frac{hc}{\lambda kT_e}\right) d\lambda, \quad (3)$$

where  $c$ ,  $k$ ,  $h$ ,  $Z$ ,  $e$ ,  $n_i$ ,  $n_e$ , and  $T_e$ , respectively, represent the speed of light, Boltzmann's constant, Planck's constant, the nuclear charge, electronic charge, the ion number density, the electron density, and the electron temperature. Furthermore, using an absorption cross section of the gas  $Q_{n,l}$  in which free electrons are captured to reach the  $(n,l)$  state, where  $n$  and  $l$ , respectively, denote the principal and the angular quantum number. The volumetric continuum emission

of free-bound radiation is expressed as<sup>23</sup>

$$j_{fb\lambda} d\lambda = \frac{2hc}{\lambda^5} Q_{n,l} n_{n,l} \exp\left(-\frac{hc}{\lambda kT_e}\right) d\lambda, \quad (4)$$

with the emission being the function of  $1/\lambda^5$  after conversion from wave number space to wavelength space. Although fitting of a continuous spectrum with absolute intensity is commonly done, estimating its intensity accurately in experiments is difficult. Therefore, the continuum spectrum was evaluated in terms of relative intensity using the Boltzmann-like plot with a logarithmic form.<sup>25</sup> The free-free and free-bound spectrum intensities  $j_{ff}$  and  $j_{fb}$  are described as

$$j_{\lambda}^{BF \text{ or } FF} = C_1 F(n_e, n_i, T_e) \frac{1}{\lambda^n} \exp\left(-\frac{hc}{\lambda kT_e}\right), \quad (5)$$

where  $C_1$  and  $F$ , respectively, represent the physical constant and the functions of  $n_e$ ,  $n_i$ , and  $T_e$ . In free-bound transition,  $n = 5$ ; in free-free transition,  $n = 2$ . The exp function and the proportional exponent of the wavelength from that equation are examined specifically below. In free-bound, it is the reciprocal of the fifth power of wavelength; in free-free, it is the reciprocal of the square of the wavelength. Based on this difference, a Boltzmann-like plot can be compiled as shown below by taking logarithms of both sides as

$$\ln\left(\frac{I_{\lambda} \lambda^n}{C_1 F}\right) = -\frac{hc}{k\lambda T_e} + C_2, \quad (6)$$

where  $C_2$  is the physical constant. Function  $F$  is a parameter of electron and ion density and electron temperature.  $T_e$  on the left-hand side is in log formula. Therefore,  $T_e$  in function  $F$  slightly affects the slope fitting analysis in Eq. (6).

#### C. Determination of electron temperature and density

Figure 5 presents spectrum time changes of the wavelengths of 400–600 nm at  $x = 0.5$  mm. The figure shows five timings of 150, 250, 450, 650, and 1050 ns, where the timing represents the elapsed time with half of the ICCD gate width (+50 ns). First, the continuous spectrum and the line spectrum of Ar I can be confirmed. Overlapping noises peculiar to the Echelle spectrometer are apparent near 400–450 nm. The emission intensity was strongest at 450 ns and it decreased over time thereafter. The local-thermodynamic equilibrium (LTE) condition can be assumed for laser-plasma. Therefore, it is common to obtain the electron temperature from the Boltzmann plot and to obtain the electron density from Stark broadening.<sup>26</sup> However, the electron temperature could not be obtained from Ar I at  $x = 0.5$  mm because the Boltzmann plot could not be obtained. Therefore, the electron temperature was calculated by fitting the theoretical equation of radiation intensity by free-free or free-bound transition. This fitting process was applied to the unaffected part of the line spectrum of 480–575 nm.

The electron temperature and spectral broadening were used to calculate the electron density considering the influence of electrons of the Stark effect.<sup>27</sup> Figure 6 shows the electron temperature and density at  $x = 0.5$  mm and  $t = 50$ –1050 ns. The continuum

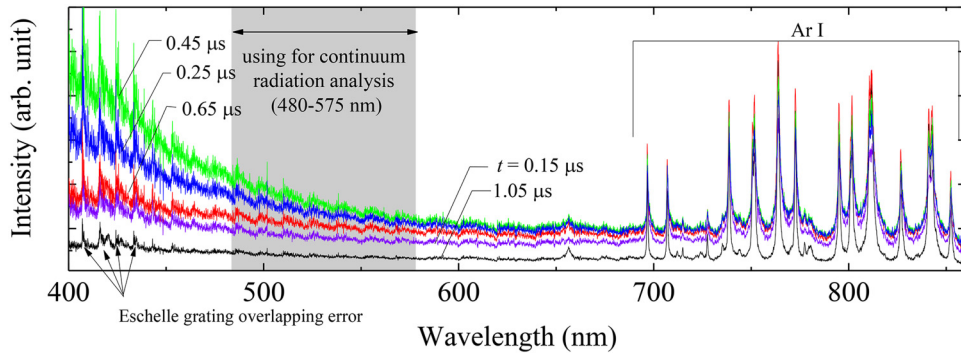


FIG. 5. Experimentally obtained Ar spectra at 400–860 nm wavelengths for  $(x, t) = (0.5 \text{ mm}, 0\text{--}1050 \text{ ns})$ , where  $x$  is the distance between the Al target and the ionization front of laser-induced plasma.

radiation fitting was performed for both free–free emission and free–bound emission. In free–free emission, the electron temperature was higher than 8 eV at  $t < 250 \text{ ns}$ . On the other hand, using free–bound emission fitting, the electron temperature was less than 1 eV. Considering the energy conservation of the electron avalanche process in the laser radiation, the electron temperature can be estimated to be about 1 eV at  $10^{11} \text{ W/m}^2$ .<sup>6</sup> As shown in Fig. 4, the temperature was estimated at 1.38 eV using Eq. (1). Considering the ICCD gate width at 100 ns, the electron temperature for  $x = 0.5 \text{ mm}$  and  $t = 50\text{--}250 \text{ ns}$  was slightly less than 1.38 eV. Therefore, the electron temperature and density were determined assuming that the continuous emission was dominated by free–bound transition. The peak of the electron temperature was 1.2 eV at  $t = 450 \text{ ns}$ . The peak of the electron density was  $2.5 \times 10^{23} \text{ m}^{-3}$  at  $t = 50 \text{ ns}$ , and the electron density was decreased with time. In the region of FIW ( $t = 50\text{--}150 \text{ ns}$ ), the electron temperature was less than 0.8 eV, and the electron number density was higher than  $2 \times 10^{23} \text{ m}^{-3}$ . At 250 ns, when the transition from FIW to LSDW appears to have occurred, the electron temperature

increased to about 1 eV, and the electron number density reaches a value of  $2.2 \times 10^{23} \text{ m}^{-3}$ . The measurement error might affect this small difference in the electron density.

Next, for comparison, the experimentally obtained Ar spectra at 400–860 nm wavelengths for the region  $x = 5 \text{ mm}$ , which is the range of LSDW, is shown in Fig. 7. From Fig. 3, the wavefront arrival is inferred as about  $1.0 \mu\text{s}$ . In fact, data were obtained for six gate delays of 1.0, 1.5, 2.0, 3.0, 4.0, and  $5.0 \mu\text{s}$ . The Ar I spectrum was only confirmed at  $t = 1.0 \mu\text{s}$ . Then, Ar I and Ar II luminescence were confirmed at  $4.0\text{--}5.0 \mu\text{s}$ . For LTE plasma in LSDW, the Boltzmann plot was applied to Ar I and Ar II to obtain the electron temperature. Figure 8 presents the electron temperature and electron density from  $1.0 \mu\text{s}$  to  $5.0 \mu\text{s}$  when LSDW reaches  $x = 5 \text{ mm}$  from the shadowgraph. Figure 9 shows the Boltzmann plot for Ar I [ $t = 1.0 \mu\text{s}$  (a) and  $1.5 \mu\text{s}$  (b)] and Ar II [ $t = 4.0 \mu\text{s}$  (c) and  $5.0 \mu\text{s}$  (d)]. As a result, the electron temperature at  $t = 1.0, 1.5, 4.0,$  and  $5.0 \mu\text{s}$  were, respectively, 0.3, 0.7, 1.9, and 2.1 eV. Using the electron temperature, the electron density was obtained from Stark broadening.<sup>27</sup> At  $t = 2.0 \mu\text{s}$  and  $3.0 \mu\text{s}$ , obtaining the Ar I Boltzmann plot was difficult. The Ar II emission and the continuum spectrum were not observed. Therefore, the electron temperature for 2.0 and  $3.0 \mu\text{s}$  was blank.

To evaluate the electron temperature deduced by the Boltzmann plot, the electron temperature was evaluated assuming  $n_i = n_e$  and using the Saha equilibrium equation and electron density,

$$\frac{n_i n_e}{n_n} = 2 \frac{g_i}{g_1} \left( \frac{2\pi m_e k T_e}{h^2} \right)^{1.5} e^{-\frac{I}{kT_e}}. \quad (7)$$

Here, the statistical weight for the ground state  $g_1$  and the ionization level  $g_i$  are, respectively, 1 and 4.<sup>23</sup>  $I$  is the first ionization energy of argon. As shown in Fig. 8, at  $t = 1.0\text{--}1.5 \mu\text{s}$ , the temperature of the Boltzmann plots is slightly less than that of the Saha equation results. At  $t = 4.0\text{--}5.0 \mu\text{s}$ , Saha equilibrium results are slightly less than the Boltzmann plot results. Results reveal that the temporal distribution of temperature is slightly increased with the time elapsed. Next, using Fig. 7, the simulated emission spectrum was obtained using the NIST LIBS database.<sup>28</sup> Figure 10 shows the simulated argon spectrum for  $(n_e, T_e) = (10^{24} \text{ m}^{-3}, 2 \text{ eV})$ ,  $(10^{23} \text{ m}^{-3}, 1.2 \text{ eV})$ , and  $(10^{23} \text{ m}^{-3}, 0.3 \text{ eV})$ . For  $(n_e, T_e) = (10^{24} \text{ m}^{-3}, 2 \text{ eV})$  at  $t = 4.0\text{--}5.0 \mu\text{s}$ , Ar I and Ar II spectra were observed in the simulated spectrum, which was similar to the experimental result in Fig. 7. For  $(10^{23} \text{ m}^{-3}, 1.2 \text{ eV})$

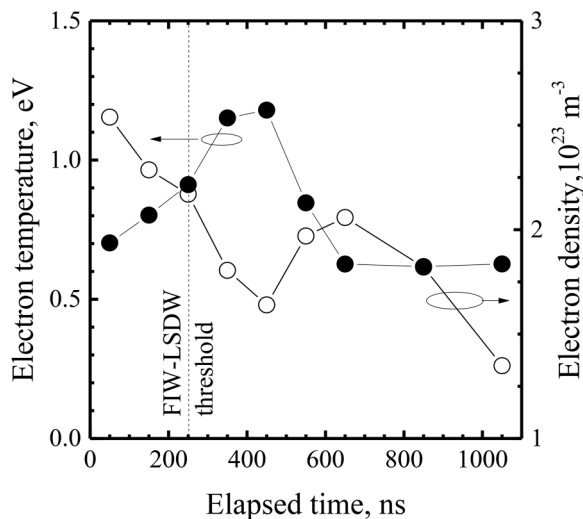


FIG. 6. Electron density and temperature for  $(x, t) = (0.5 \text{ mm}, 0\text{--}1050 \text{ ns})$ .

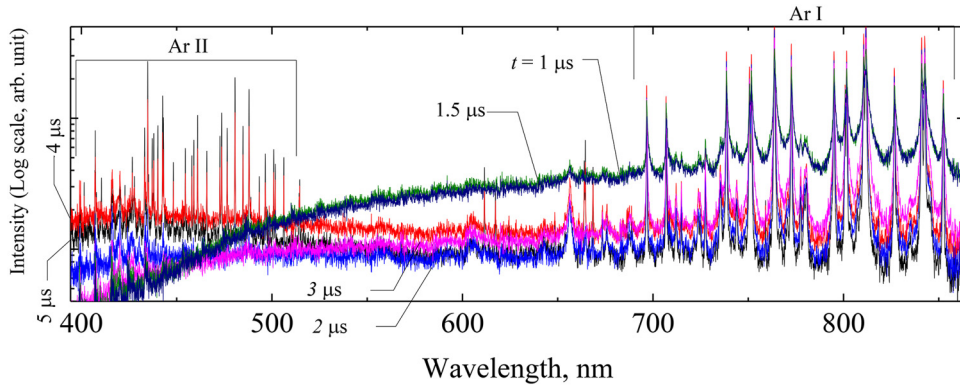


FIG. 7. Experimentally obtained Ar spectra at 400–860 nm wavelengths for  $(x, t) = (5 \text{ mm}, 1\text{--}5 \mu\text{s})$ .

and  $(10^{23} \text{ m}^{-3}, 0.3 \text{ eV})$ , the Ar I spectrum was only observed; however, the difference of intensity was 14 orders of magnitude. The electron temperature at  $t = 1.0 \mu\text{s}$  can be estimated to be about 1 eV as shown in the Saha equilibrium of Eq. (7) and the Raizer estimation of Fig. 4 because the intensity of the observed spectrum at  $t = 1.0 \mu\text{s}$  was almost the same as that at  $t = 5.0 \mu\text{s}$ , as can be seen from Fig. 7. The results reveal that the result of the Boltzmann plot underestimated the electron temperature at  $t = 1.0 \mu\text{s}$  due to the nonequilibrium plasma condition.

#### IV. VALIDITY OF LOCAL-THERMODYNAMIC EQUILIBRIUM

As described in Sec. III, the plasma condition behind the LSDW front was difficult to use in the Boltzmann plot technique, which can be considered for the same plasma condition in FIW because of the same electron temperature and density. Therefore, the

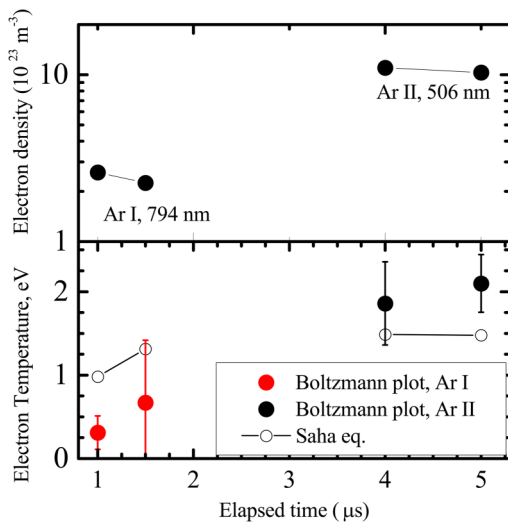


FIG. 8. Electron density and temperature for  $(x, t) = (5 \text{ mm}, 1\text{--}5 \mu\text{s})$ .

collision frequencies of electrons and neutrals were obtained from the obtained electron temperature and density to investigate the energy relaxation process and equilibrium in plasma. Specifically, for the inelastic collision between the electron and neutral particles (e-n), the Ar I excited level of  $3p^5 4s$ ,  $3p^5 4p$ , and  $3p^5 3d$  was considered.<sup>29</sup> As shown in Figs. 5 and 10, the observed Ar I spectrum in the range of 600–900 nm are mainly caused by the fine structure of  $3p^5 4s$  and  $3p^5 4p$ . The relaxation times of different excited levels ( $i$ ) are expressed as

$$\tau_{en,i} = \frac{1}{n_e K(i) + A(i)}, \quad (8)$$

where  $K(i)$  and  $A(i)$  are, respectively, the total rate of collisional destruction and the effective radiative decay rate of level  $i$ .<sup>30,31</sup> Figure 11 shows the electron-neutral energy relaxation time for elastic and inelastic collisions as a function of electron temperature. Each relaxation time is normalized by the electron-electron (e-e) collision relaxation time. As shown in Figs. 11(a) and 11(b), each relaxation time satisfies the following relation at  $T_e = 0.3\text{--}1.0 \text{ eV}$  for  $n_e = 10^{23} \text{ m}^{-3}$  obtained by near wavefronts of FIW and LSDW, and  $T_e = 2 \text{ eV}$  for  $n_e = 10^{24} \text{ m}^{-3}$  far behind the LSDW wavefront,

$$\tau_{ee} < \tau_{en,elastic} \ll \tau_{en,inelastic(4s,4p,3d)}.$$

Results revealed that the energy relaxation from the laser electric field to electrons occurs, and then the electron energy is gradually relaxed in the heavy particles. Although in Fig. 11(b), the plasma is in the LTE condition, and there is no clear difference between Figs. 11(a) and 11(b). To validate the existence of LTE in plasma, the McWhirter criterion is most popularly used in the LIBS literature.<sup>26,32</sup> The criterion assumes that the collision-induced transition rates are about 10 times higher than the radiative decay rate. The criterion is expressed as<sup>33</sup>

$$n_e > 1.6 \times 10^{16} T_e^{0.5} (\Delta E_{ij})^3, \quad (9)$$

where  $T_e$  and  $\Delta E_{ij}$  are expressed in Kelvin and electron volt, respectively. For transition between the ground level to  $3p^5 4s$  (11 eV) and  $3p^5 4p$  (13 eV) when  $T_e = 1 \text{ eV}$ , the criterion  $n_e$  are, respectively,

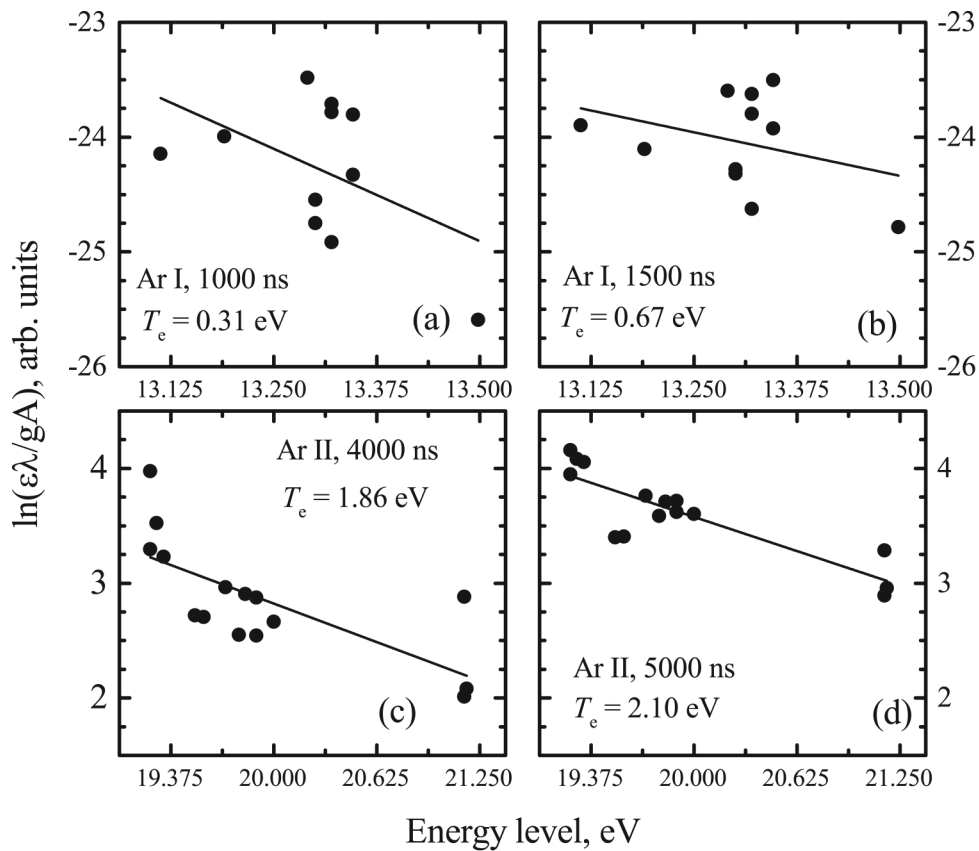


FIG. 9. Boltzmann's plot analysis for Ar I [ $t = 1 \mu\text{s}$  (a),  $1.5 \mu\text{s}$  (b)] and Ar II [ $4 \mu\text{s}$  (c),  $5 \mu\text{s}$  (d)].

$2.3 \times 10^{23} \text{ m}^{-3}$  and  $3.8 \times 10^{23} \text{ m}^{-3}$ . These results are close to the obtained  $n_e = 3 \times 10^{23} \text{ m}^{-3}$ . The McWhirter criterion reveals that the existence of LTE in plasma behind LSDW, or even FIW, was not clearly satisfied in the experimental condition. Consequently, the electron temperature near the front of LSDW was uncertainty estimated by the Boltzmann plot and the Saha equilibrium technique. Further investigation is necessary to understand the nonequilibrium plasma condition and their energy relaxation mechanism and to obtain the exact electron temperature for LSDW.

### V. THEORETICAL ESTIMATION OF TRANSITION BETWEEN FIW AND LSDW

Finally, the threshold was estimated using Fisher's transition threshold model and the electron temperature inferred as described in Sec. IV. The transition threshold  $q_{\text{thr}}$  ( $\text{W}/\text{m}^2$ ) is expressed as

$$q_{\text{thr}}(T_e) = \frac{m c \epsilon_0}{e} (\omega^2 + \nu_c^2) \left\{ \left( E_e + \frac{3}{2} T_e \right) \frac{\ln(n_e/n_{\text{ph}})}{\nu_c \tau_L} + \frac{3m}{M} (T_e - T_h) \right\}, \quad (10)$$

where  $\nu_c$  and  $n_{\text{ph}}$ , respectively, represent the frequency of elastic collisions of the electrons and the electron number density inferred from the photoionization process.<sup>6</sup> The electron energy  $E_e$  is defined as being within the range of  $E_{e,\text{ex}} < E_e < E_{e,\text{ion}}$ . It is noteworthy that  $E_{e,\text{ex}}$  and  $E_{e,\text{ion}}$ , respectively, denote the potentials of the first excited energy level and the ionization threshold (15.76 eV). The first excited state of argon,  $3p^5 4s$ , lies approximately 11.55 eV above the ground state.  $n_{\text{ph}}$  is the function of the plasma radiation, the photoabsorption cross section, and the geometrical condition. To avoid the uncertainty radiation calculation, the term  $\ln(n_e/n_{\text{ph}})$  was evaluated using the avalanche time constant.<sup>6</sup> Besides,  $T_e \gg T_h$  was assumed in the second term of the right-hand side. Consequently,  $q_{\text{thr}}$  is possible to estimate using the electron temperature. Assuming the electron temperature was 1 eV ( $t = 250 \text{ ns}$ ),  $q_{\text{thr}}$  is estimated to be in the range of  $2.6 \times 10^{11} \text{ W}/\text{m}^2 < q_{\text{thr}} < 3.4 \times 10^{11} \text{ W}/\text{m}^2$ . Although the calculation results agree with the experimental values in order of the magnitude, it is difficult to obtain more accurate analysis using the simple electron energy equation. The details of propagation and transition of FIW can be understood by the numerical simulation considering the radiation transportation and laser-plasma interaction

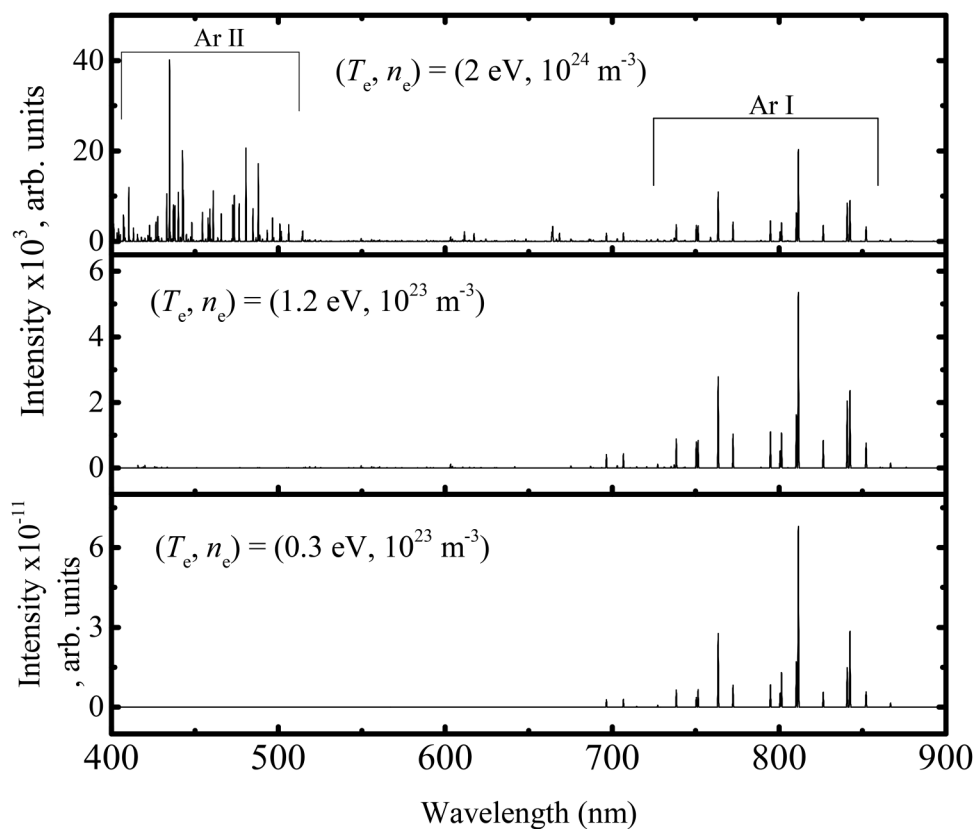


FIG. 10. Simulated argon spectrum for  $(n_e, T_e) = (10^{24} \text{ m}^{-3}, 2 \text{ eV})$ ,  $(10^{23} \text{ m}^{-3}, 1.2 \text{ eV})$ , and  $(10^{23} \text{ m}^{-3}, 0.3 \text{ eV})$ .

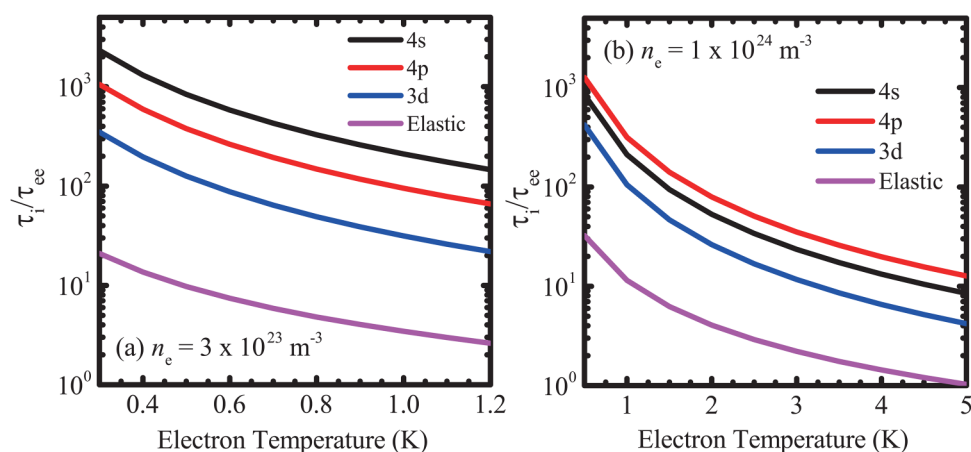


FIG. 11. Relaxation time of electron-neutral particle for elastic and inelastic collisions as a function of electron temperature: (a)  $n_e = 3 \times 10^{23} \text{ m}^{-3}$  and (b)  $n_e = 1 \times 10^{24} \text{ m}^{-3}$ . Each relaxation time is normalized by the electron-electron (e-e) collision relaxation time.

## VI. CONCLUSION

As described in this paper, emission spectroscopy was used to elucidate the FIW–LSDW transition phenomena. High-speed visualization and emission spectroscopy were applied to LSDW for comparison with FIW. The FIW–LSDW transition is detectable from the shadowgraph and CJ-detonation theory related to shadowgraphy conducted with a high-speed camera. As a result, the laser intensity and the ionization front velocity at the threshold were, respectively,  $1.0 \times 10^{11} \text{ W/m}^{-2}$  and 5 km/s in the argon gaseous form. It was not possible to confirm a clear change in the FIW–LSDW transition from the shadowgraph results. Next, emission spectroscopic measurements were conducted to the Ar plasma for FIW and LSDW. In FIW measurements, the Boltzmann plot is difficult to apply. Instead, the electron temperature and density were calculated from the continuous spectrum and the line spectrum of ArI. At  $x = 0.5 \text{ mm}$ , results show that the emission intensity was maximum at 450 ns, the electron temperature was highest at 450 ns and 1.2 eV, and the electron density was maximum at  $t = 50 \text{ ns}$ . The plasma behind the FIW wavefront,  $t = 50\text{--}150 \text{ ns}$ , was found to have an electron temperature of 0.7 eV and an electron number density of  $2.5 \times 10^{23} \text{ m}^{-3}$ . For LSDW, the electron temperature was about 1 eV behind the wavefront, and the electron density was about  $2.7 \times 10^{23} \text{ m}^{-3}$ . At the threshold of FIW and LSDW, the electron temperature and density were, respectively, 0.3–1.0 eV and  $2.2 \times 10^{23} \text{ m}^{-3}$ . The plasma in the near LTE condition for LSDW affects the relatively wide range value of electron temperature. Using Fisher's theory and the obtained electron temperature, the laser intensity at the threshold between the FIW and LSDW was estimated to be the range of  $(2.6\text{--}3.4) \times 10^{11} \text{ W/m}^2$ .

## ACKNOWLEDGMENTS

This work was supported by the Tanikawa Fund, Promotion of Thermal Technology.

## REFERENCES

- <sup>1</sup>R. G. Root, "Modeling of post-breakdown phenomena," in *Laser-Induced Plasmas and Applications*, edited by L. J. Radziemski and D. A. Cremers (Marcel Dekker, New York, 1989), Chap. 2.
- <sup>2</sup>A. A. Ilyin, I. G. Nagorny, and O. A. Bukin, *Appl. Phys. Lett.* **96**, 171501 (2010).
- <sup>3</sup>V. I. Fisher, *Sov. Phys. JETP* **52**, 1083 (1980).
- <sup>4</sup>V. I. Fisher, *Sov. Phys. JETP* **79**, 2142 (1980).
- <sup>5</sup>V. I. Fisher, *Sov. Phys. Tech. Phys.* **28**, 1312 (1983).
- <sup>6</sup>V. I. Fisher, *Sov. Phys. JETP* **56**, 1004 (1982).
- <sup>7</sup>M. B. Zheleznyak, A. K. Mnatsakanyan, and S. V. Sizykh, *High Temp.* **20**, 423 (1982).
- <sup>8</sup>E. M. Bazelyan and Y. P. Raizer, *Spark Discharge* (CRC Press, 1997).
- <sup>9</sup>J. P. Davis, A. L. Smith, C. Giranda, and M. Squicciarini, *Appl. Opt.* **30**, 4358 (1991).
- <sup>10</sup>S. S. Harilal, *Appl. Opt.* **43**, 3931 (2004).
- <sup>11</sup>C. V. Bindhu, S. S. Harilal, M. S. Tillack, F. Najmabadi, and A. C. Gaeris, *Appl. Spectrosc.* **58**, 719 (2004).
- <sup>12</sup>Y.-L. Chen, J. W. L. Lewis, and C. Parigger, *J. Quant. Spectrosc. Radiat. Transfer* **67**, 91 (2000).
- <sup>13</sup>S. V. Zakharchenko, *Sov. J. Quantum Electron.* **14**, 1429 (1984).
- <sup>14</sup>V. A. Boiko, V. A. Danilychev, B. N. Duvanov, V. D. Zvorykin, and I. V. Holin, *Sov. J. Quantum Electron.* **5**, 216 (1978).
- <sup>15</sup>I. Z. Nemtsev and B. F. Mulchenko, *Sov. J. Plasma Phys.* **3**, 649 (1977).
- <sup>16</sup>J. Camacho, M. Santos, L. Diaz, L. J. Juan, and J. M. L. Poyato, *Appl. Phys. A* **99**, 159 (2010).
- <sup>17</sup>K. Shimamura *et al.*, *Appl. Phys. Lett.* **110**, 134104 (2017).
- <sup>18</sup>K. Shimamura *et al.*, *J. Appl. Phys.* **109**, 084910 (2011).
- <sup>19</sup>K. Mori, K. Komurasaki, and Y. Arakawa, *Appl. Phys. Lett.* **88**, 121502 (2006).
- <sup>20</sup>Y. P. Raizer, *Sov. Phys. JETP* **21**, 1009 (1965).
- <sup>21</sup>K. Mori, K. Komurasaki, and Y. Arakawa, *J. Appl. Phys.* **92**, 5663 (2002).
- <sup>22</sup>Y. B. Zel'dovich and Y. P. Raizer, *Physics of Shock Waves and High-Temperature Hydrodynamic Phenomena* (Dover Publications, New York, 2002).
- <sup>23</sup>T. K. Bose, *High Temperature Gas Dynamics: An Introduction for Physicists and Engineers*, 2nd ed. (Springer, New York, 2014).
- <sup>24</sup>M. G. Kapper and J.-L. Cambier, *J. Appl. Phys.* **109**, 113308 (2011).
- <sup>25</sup>A. De Giacomo, R. Gaudioso, M. Dell'Aglio, and A. Santagata, *Spectrochim. Acta B* **65**, 385 (2010).
- <sup>26</sup>D. A. Cremers and L. J. Radziemski, *Handbook of Laser-Induced Breakdown Spectroscopy*, 2nd ed. (John Wiley & Sons Ltd, 2013).
- <sup>27</sup>H. R. Griem, *Spectral Line Broadening by Plasmas* (Academic Press, New York, 1974).
- <sup>28</sup>See <https://physics.nist.gov/PhysRefData/ASD/LIBS/lib-form.html> for "NIST LIBS Database."
- <sup>29</sup>F. F. Chen, *Introduction to Plasma Physics and Controlled Fusion*, 3rd ed. (Springer, 2016).
- <sup>30</sup>G. Colonna *et al.*, *Spectrochim. Acta B* **56**, 587–598 (2001).
- <sup>31</sup>J. A. M. van der Mullen, *Phys. Rep.* **191**, 109–220 (1990).
- <sup>32</sup>G. Christoforetti *et al.*, *Spectrochim. Acta B* **65**, 86–95 (2010).
- <sup>33</sup>R. W. P. McWhirter, in *Plasma Diagnostic Techniques*, edited by R. H. Huddleston and S. L. Leonard (Academic Press, New York, 1965).